FRONTIERS OF PHYSICS

RESEARCH ARTICLE
Volume 21 / Issue 9 / 096201 / 2026

Constraining cross sections for unstable ^{153,159}Gd(n, γ) and their astrophysical implications

Shu-Tong Zhang [1,2], Zhi-Cai Li[1,2,†], Kai-Jun Luo[1,2], Hong-Chen Liu[1,2], Yun-Jie Guo[3,‡], Kai-Xin Zhao[1,2], Zi-Ang Lin[1,2], Wen Luo[1,2,§]

1 School of Nuclear Science and Technology, University of South China, Hengyang 421001, China
2 Key Laboratory of Advanced Nuclear Energy Design and Safety, Ministry of Education, Hengyang 421001, China
3 Office of the Financial Commission, CPC Hunan Provincial Committee, Changsha 410011, China
Corresponding authors. E-mail: †lizhicai@usc.edu.cn, ‡413454945@qq.com, §wenluo-ok@163.com
Received February 5, 2026; accepted May 2, 2026

ABSTRACT

Neutron capture (n, γ) cross sections of gadolinium (Gd) isotopes are critical to astrophysics research, nuclear reactor designs, and medical applications. However, the available (n, γ) data on unstable Gd isotopes are scarce and direct measurement is challenging. In this work, we propose an approach to infer the (n, γ) cross sections for unstable ^{153,159}Gd isotopes by constraining both the γ-ray strength functions (γSFs) and nuclear level densities (NLDs). Specifically, the key γSF parameters are adjusted to match the available experimental data, and the NLD parameters are determined by renormalizing microscopic level densities through a Bayesian optimization method. Our approach is verified by comparing our predictions with the experimental (n, γ) data for the stable ^{155,157}Gd isotopes. We then infer the unstable ^{153,159}Gd(n, γ) cross sections within the neutron energy range of 0.01–5.0 MeV. The resulting uncertainty intervals are evaluated to be 23.5%–40.4% for ^{153}Gd and 30.8%–51.1% for ^{159}Gd, which are about two times smaller than those obtained without experimental constraints. We further calculate the astrophysical reaction rates for the ^{153,159}Gd isotopes. It is found that the ^{159}Gd(n, γ) rate is larger by a factor of $\sim$2.9 than the JINA REACLIB recommendation. This suggests a larger branching ratio for ^{159}Gd and may result in a visible increase in the ^{160}Gd abundance through neutron capture reaction. Our approach is promising for constraining (n, γ) data for a wider range of unstable isotopic chains and for improving astrophysical reaction-network calculations and related nuclear-science applications.

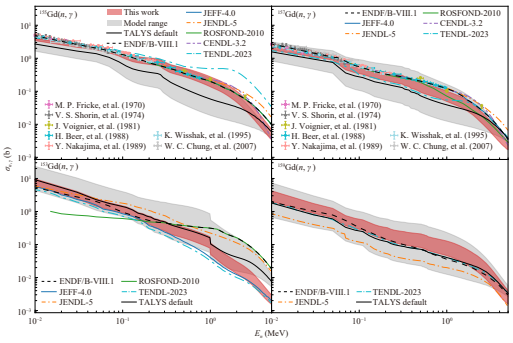

Keywords gadolinium isotopes, neutron capture cross section, gamma-ray strength function, nuclear level density, astrophysical reaction rate, *s*-process nucleosynthesis

1 Introduction

Most of the elements heavier than iron are produced by a sequence of neutron capture reactions and β-decays during different phases of stellar evolution. The two dominant processes involved are the rapid (r) and the slow (s) neutron capture processes [1–4]. In particular, unlike most of the isotopes, ^{152}Gd and ^{154}Gd receive

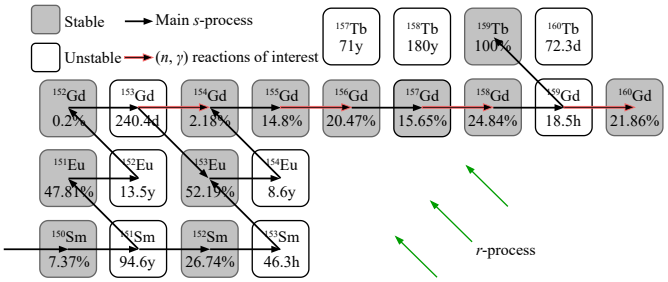

Fig. 1 Simplified nucleosynthesis path of Sm, Eu, Gd, and Tb during the s-process. Stable isotopes are shown in grey, while unstable isotopes are in white. Their natural abundances or half-lives are listed accordingly. The black arrows indicate the main s-process flow. The red-framed black arrows indicate the (n,γ) reactions of interest investigated in this work.

contributions only from the s-process. These so-called "s-only" isotopes are crucial for testing s-process models. As illustrated in Fig. 1, they are shielded against the β-decay chains from the r-process region by stable samarium isobars [4–6]. The determination of their final abundances, however, crucially depends on the branchings at unstable nuclei, where neutron-capture rates compete with β-decay rates [5, 7]. In the standard s-process, the branching at unstable isotope ^{153}Gd is relatively minor [5]. In contrast, under the higher neutron density conditions of the intermediate neutron capture process (i-process), the contribution from ^{153}Gd(n,γ) may become non-negligible. Similarly, a comparable situation exists for the unstable isotope ^{159}Gd, which thus requires further analysis. Furthermore, ^{155}Gd and ^{157}Gd account for the majority of the natural Gd cross section, with ^{157}Gd notably possessing the highest thermal cross section of 254,000 barns, making them pivotal for reactor designs and medical applications such as Gadolinium Neutron Capture Therapy [8–10]. Consequently, obtaining reliable neutron capture cross sections and reaction rates for Gd isotopes is critical for stellar nucleosynthesis models, reactor designs, and medical applications.

While experimental cross section data for stable Gd isotopes are generally available, experimental data for the crucial unstable isotopes ^{153}Gd and ^{159}Gd are scarce and direct measurements remain extremely challenging. Specifically, measurements involving radioactive targets are hindered by the high radioactivity of the samples. Furthermore, experiments in inverse kinematics are currently not feasible for (n,γ) reactions because free-neutron targets are not available [11, 12]. In the absence of experimental data, most neutron capture cross sections and reaction rates required for stellar modeling rely heavily on theoretical model predictions. However, these predictions often suffer from large uncertainties due to difficulties in accurately describing the deexcitation process of the nucleus formed after neutron capture. Indeed, this process is ruled by fundamental nuclear properties (γ-ray strength functions (γSF), nuclear level densities (NLD), etc.), for which existing nuclear models yield widely conflicting results in the absence of experimental constraints. As a result, the predicted cross sections can exhibit significant divergence, reaching variations of up to several orders of magnitude [13–16]. Consequently, these theoretical uncertainties propagate directly into astrophysical reaction rates, limiting the reliability of nucleosynthesis simulations for unstable isotopes. To reduce these uncertainties, indirect approaches have become an important alternative when direct (n,γ) measurements are not feasible [11, 12, 17–20].

In this work, we present an effective approach to infer the (n,γ) cross sections for unstable ^{153,159}Gd isotopes by constraining both the γSFs and NLDs. The constrained γSFs and NLDs are implemented in the nuclear reaction code TALYS-2.0 [21]. We validate the approach using the stable isotopes ^{155,157}Gd, for which experimental data are available, and then infer the (n,γ) cross sections for the unstable isotopes ^{153,159}Gd. Furthermore, we calculate the resulting astrophysical reaction rates for ^{153,159}Gd and explore the implications for the s-process branching at ^{159}Gd and the production of ^{160}Gd. The remainder of this paper is structured as follows: In Section 2, we detail our approach for constraining the γSF and NLD parameters. In Section 3, we validate our approach using stable ^{155,157}Gd and present the calculated (n,γ) cross sections for the unstable ^{153,159}Gd isotopes. In Section 4, we discuss the astrophysical implications, including the reaction rates for ^{153,159}Gd, the s-process branching at ^{159}Gd, and the impact on the production of ^{160}Gd. In Section 5, we conclude and provide an outlook.

2 Extraction of γ-ray strength function and nuclear level density

2.1 $E1$ γ-ray strength function

The γSF is important for the description of any transition involving gamma rays in nuclear reactions, providing essential information for predicting capture cross sections, γ-ray production spectra, and competition between γ-ray and particle emission [22]. In this section, we extract the $E1$ γSF parameters for the ^{154,156,158,160}Gd isotopes, which serve as the compound nuclei for the neutron capture reactions calculated in this work. These parameters are constrained using experimental γSF data from the IAEA Photon Strength Function Database [23], derived from photo-absorption and photo-neutron cross section measurements [24–28]. Specifically, we use the data in the giant dipole resonance (GDR) region above the neutron separation energy (S_n) to extract the E1 γSF parameters.

The Standard Lorentzian (SLO) model [29, 30] is probably the most widely adopted approach for describing photo-absorption data of medium-weight and heavy

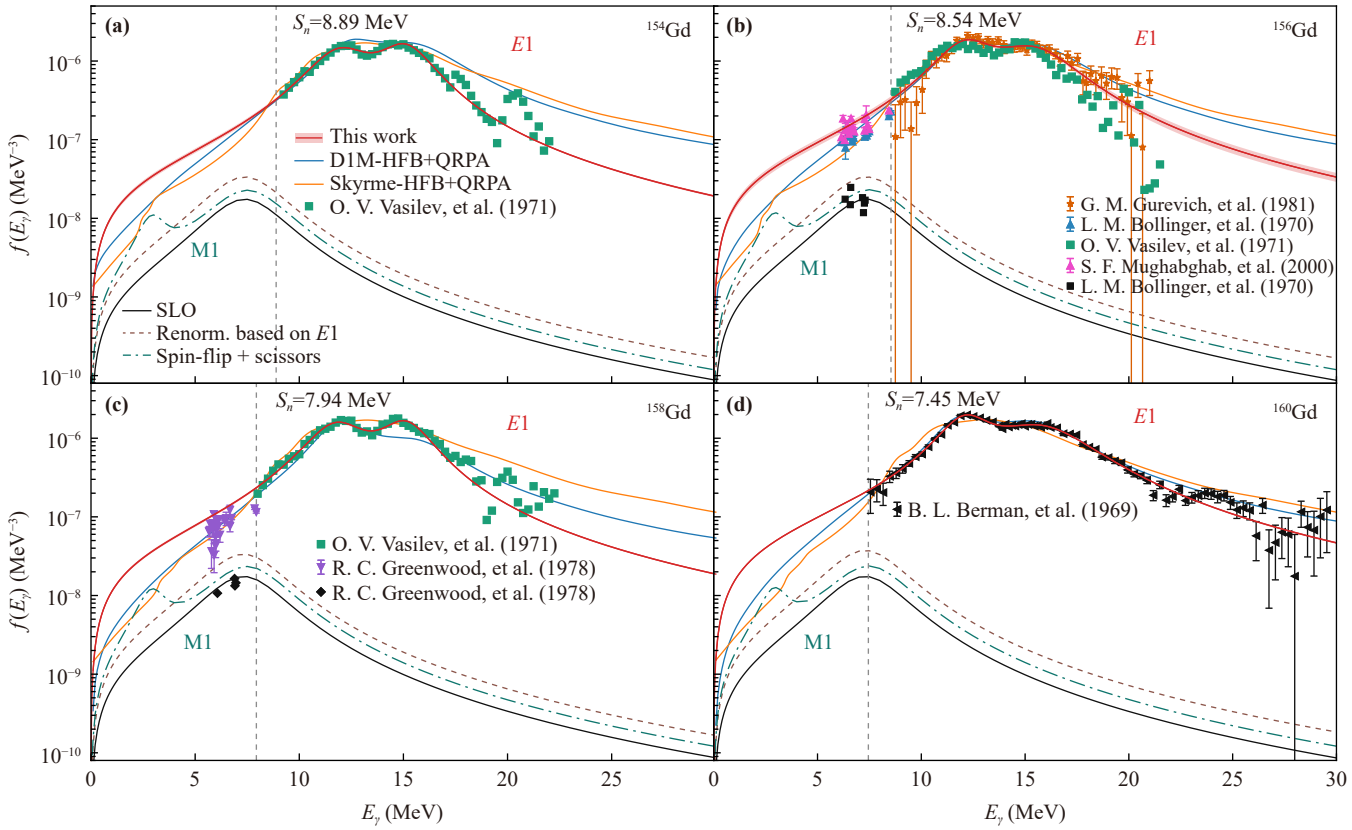

Fig. 2 **(a–d)** present the $E1$ and $M1$ γSFs for ^{154,156,158,160}Gd. For the $E1$ component, our fitted results are shown by the red curves with one-standard-deviation uncertainty bands. These are compared with the experimental γSF from Refs. [24–28] and microscopic model evaluations (D1M-HFB+QRPA [37] and Skyrme-HFB+QRPA [36], depicted by blue and orange lines, respectively). For the $M1$ component, the three adopted model prescriptions, namely the SLO, renormalized based on $E1$, and spin-flip + scissors models, are shown by the black solid, brown dashed, and green dash-dotted curves, respectively, together with the available experimental data. The vertical dashed lines indicate the S_n for each isotope.

nuclei [31–33]. The SLO form for the γ-ray strength is given by

$$f_{X\ell}(E_\gamma) = K_{X\ell} \sum_{i=1}^{N_{\rm peak}} \frac{\sigma_i E_\gamma \Gamma_i^2}{(E_\gamma^2 - E_i^2)^2 + E_\gamma^2 \Gamma_i^2}, \quad (1)$$

where $K_{X\ell} = [(2\ell+1)\pi^2(\hbar c)^2]^{-1}$, X denotes either electric (E) or magnetic (M) radiation, and ℓ is the multipolarity of the transition. E_i, Γ_i, and σ_i denote the centroid energy, width, and peak cross section of the i-th resonance, respectively. According to the Reference Input Parameter Library (RIPL-3, Ref. [22]), nuclei with a quadrupole deformation parameter $\beta_2 > 0.01$ are considered to be deformed. The Gd isotopes studied here have relatively large β_2 values ranging from 0.30 to 0.35 [34]. For such deformed nuclei, their GDR shapes are generally described by two resonance components [27, 35]. As a result, the $E1$ γSF in Eq. (1) is parameterized with two Lorentzian components ($N_{\rm peak} = 2$).

The parameter set is $\theta = (\sigma_1, E_1, \Gamma_1, \sigma_2, E_2, \Gamma_2)$, and it was determined by minimizing the chi-square defined as

$$\chi^2(\theta) = \sum_k \frac{[f_{\rm exp}(E_k) - f_{E1}(E_k;\theta)]^2}{\sigma_k^2}, \quad (2)$$

where $f_{\rm exp}(E_k)$ is the experimental γSF value at the k-th energy point E_k, and σ_k is the corresponding experimental uncertainty. The minimization was performed using nonlinear least-squares method.

Figure 2 shows our $E1$ γSF fits for ^{154,156,158,160}Gd compared with two microscopic predictions: the Skyrme-HFB+QRPA strength [36] and the D1M-Gogny HFB+QRPA strength [37]. The fitted curves reproduce the experimental data well over the GDR energy range. In contrast, the microscopic QRPA predictions reproduce the gross trend. However, they systematically underestimate the peak magnitude near the GDR centroids and overestimate the strength on the high-energy tail. The peak parameters extracted from our fits are listed in Table 1. However, due to the lack of direct measurements below the S_n, the low-energy $E1$ γSF remains an additional source of uncertainty that requires further experimental constraints.

The fitted parameters show systematic trends across

Table 1 Summary of the fitted SLO γSF parameters for ^{154,156,158,160}Gd, grouped by peak index. The uncertainties represent one standard deviation.

(i) Peak 1 parameters			
Isotope	σ_1 (mb)	E_1 (MeV)	Γ_1 (MeV)
^{154}Gd	171.23±10.15	12.09±0.12	3.25±0.27
^{156}Gd	204.74±23.77	12.24±0.18	3.06±0.46
^{158}Gd	189.61±9.73	11.90±0.10	3.15±0.18
^{160}Gd	213.10±6.77	12.21±0.04	2.71±0.13
(ii) Peak 2 parameters			
Isotope	σ_2 (mb)	E_2 (MeV)	Γ_2 (MeV)
^{154}Gd	241.56±13.97	15.12±0.09	2.81±0.15
^{156}Gd	226.48±17.66	15.51±0.21	4.35±0.55
^{158}Gd	245.38±12.75	15.13±0.08	2.72±0.13
^{160}Gd	233.92±3.86	15.93±0.06	5.37±0.14

the Gd isotopic chain. The central energies E_1 and E_2 are relatively stable at approximately 12 MeV and 15 MeV, respectively. This two-peak structure is a characteristic feature of the GDR splitting in prolate deformed nuclei, where E_1 is attributed to oscillations along the nuclear symmetry axis and the higher-energy peak E_2 to oscillations perpendicular to it. The σ_2 is generally greater than σ_1 due to the difference in the degrees of freedom for these two oscillation modes. The widths, Γ_1 and Γ_2, ranging from 2.7 to 5.4 MeV, reflect the intrinsic damping of the collective dipole motion [32, 38].

2.2 $M1$ γ-ray strength function

Although $E1$ transitions dominate the γSF, the $M1$ component may also contribute non-negligibly in the 2–10 MeV region and affects neutron capture cross sections. We consider three phenomenological $M1$ models, and their impact on the calculated cross sections is discussed in Section 3.

(i) SLO model. This prescription corresponds to the `strengthM1 1` option in TALYS. It adopts the RIPL-3 systematic formulae [22] for the $M1$ resonance parameters:

$$f_{M1}(E_\gamma = 7\ \text{MeV}) = 1.58 \times 10^{-9} A^{0.47}, \quad E_{M1} = 41\, A^{-1/3}\ \text{MeV}, \quad \Gamma_{M1} = 4\ \text{MeV}, \tag{3}$$

where A is the mass number, the σ_{M1} is determined by inverting Eq. (1) at $E_\gamma = 7$ MeV. This prescription serves as the default $M1$ input for TALYS calculations.

(ii) Renormalization based on $E1$ strength. This prescription corresponds to the `strengthM1 2` option in TALYS. It utilizes the empirical coefficient $0.0588\, A^{0.878}$ given in the RIPL-2 handbook [39] to normalize the $M1$ strength:

$$f_{M1}(E_\gamma) = \frac{f_{E1}(E_\gamma)}{0.0588\, A^{0.878}}. \tag{4}$$

(iii) Spin-flip and scissors-mode. This prescription corresponds to the `strengthM1 3` option in TALYS. It models the total $M1$ strength as a superposition of two components. The Spin-flip component represents a broad resonance parameterized based on the nuclear mass. In contrast, the Scissors mode accounts for the extra strength observed in the $E_\gamma \sim 2$–4 MeV region. The scissors mode was first predicted by Iudice and Palumbo [40] within a semiclassical two-rotor model. This collective excitation mode was subsequently observed experimentally in ^{156}Gd by Bohle *et al.* [41] Since its strength is directly proportional to β_2, for the deformed Gd nuclei studied here ($\beta_2 \approx 0.3$–0.35) this low-energy contribution cannot be neglected [42].

As shown in Fig. 2, these three $M1$ prescriptions are compared explicitly with the available experimental data. For the renormalization based on $E1$ strength [method **(ii)**], the calculation uses the best-fit $E1$ parameters from Table 1. All three models exhibit a resonance peak centered near $E_\gamma \approx 7.6$ MeV, with the method **(i)** predicting the lowest strength and the second model predicting the highest. The third model is distinguished by an additional pronounced enhancement in the low-energy region, $E_\gamma \sim 2$–4 MeV. Such a low-energy upturn can impact the capture calculations. These differences, particularly at low energies, illustrate the model uncertainty in the $M1$ strength function. This uncertainty propagates to the (n,γ) cross section calculations.

2.3 Nuclear level density normalization

At the neutron-separation energy S_n, the average s-wave neutron-resonance spacings D_0 [22] are usually used to calculate the total level density $\rho(S_n)$. For the case of Gd, there are no experimental D_0 data for ^{160}Gd, because ^{159}Gd is unstable. To estimate a reasonable D_0

for ^{160}Gd, we considered systematics of s-wave resonance spacings for this mass region by using the most recent evaluation of the RIPL-3. In addition, to determine $\rho(S_n)$, systematic errors arising from the spin distribution at S_n must be reasonably accounted for [43].

Following Refs. [44, 45], we first describe the excitation-energy dependence of the spin-cutoff parameter σ^2 with two phenomenological Fermi-gas (FG) prescriptions. We first introduce the rigid-body approximation of Ref. [44], which reads (FG05):

$$\sigma^2_{\mathrm{FG05}}(E_x) = 0.0146\,A^{5/3}\frac{1+\sqrt{1+4a\,(E_x-E_1)}}{2a}, \quad (5)$$

where E_x is the excitation energy, a is the NLD parameter, and E_1 is the excitation-energy back-shift determined from global systematics of Ref. [44]. We then consider the FG spin-cutoff parameter of Ref. [45] (FG09):

$$\sigma^2_{\mathrm{FG09}}(E_x) = 0.391\,A^{0.675}\left(E_x-\frac{1}{2}Pa^*\right)^{0.312}, \quad (6)$$

with Pa^* denoting the pairing energy for deuteron as defined in Ref. [45]. For the phenomenological σ^2, the spin distribution is given by the standard expression [46]:

$$g(E_x,J) = \frac{2J+1}{2\sigma^2(E_x)}\exp\left[-\frac{(J+\frac{1}{2})^2}{2\sigma^2(E_x)}\right], \quad (7)$$

where J is the spin of the levels at E_x. By using the phenomenological spin-cutoff parameters and assuming equal parity populations at S_n, the total level density is obtained from D_0 through

$$\rho(S_n) = \frac{2\,\sigma^2(S_n)/D_0}{(J_\mathrm{t}+1)\exp\left[-\frac{(J_\mathrm{t}+1)^2}{2\sigma^2(S_n)}\right]+J_\mathrm{t}\exp\left[-\frac{J_\mathrm{t}^2}{2\sigma^2(S_n)}\right]}, \quad (8)$$

where J_t is the ground-state spin of the target nucleus.

For the ^{154,156,158,160}Gd nuclei, we investigated the spin distribution using σ^2_{FG05}, σ^2_{FG09}. We observe that the spin distribution calculated using σ^2_{FG05} is significantly broader and centered at higher spins compared to that using σ^2_{FG09}. This finding is consistent with the results reported by Larsen *et al.* [43]. Therefore, we consider ρ_{FG05} (calculated using σ^2_{FG05}) as the upper limit and ρ_{FG09} (calculated using σ^2_{FG09}) as the lower limit. Consequently, we establish an uncertainty range for $\rho(S_n)$ using ρ_{FG05} and ρ_{FG09}. Based on this, we adopt the HFB+c level densities, which are renormalized to reproduce the known discrete levels and the $\rho(S_n)$ derived from Eq. (8).

As mentioned before, the experimental D_0 data for ^{160}Gd is unavailable. Given the limited experimental D_0 data for the Gd isotopic chain, we estimate it by a linear fit of $\ln(D_0)$ versus A using these neighboring nuclei (Eu, Gd, Tb) from RIPL-3. As shown in Fig. 3, a strong odd-even effect is observed in the D_0 systematics. Therefore, separate fits were performed for odd-A and even-A nuclei. For ^{160}Gd, the even-A fit yields $D_0 = 7.8 \pm 2.4$ eV. As a validation, we derived a theoretical D_0 value for ^{160}Gd based on the $\rho(S_n)$ predicted by the microscopic HFB+c model, which is consistent with the linearly extrapolated result within the 1σ uncertainty. Subsequently, with this estimated value and the experimental D_0 for the other isotopes, we calculated $\rho(S_n)$ for ^{154,156,158,160}Gd using Eq. (8), with spin cutoff parameters from Eqs. (5) and (6).

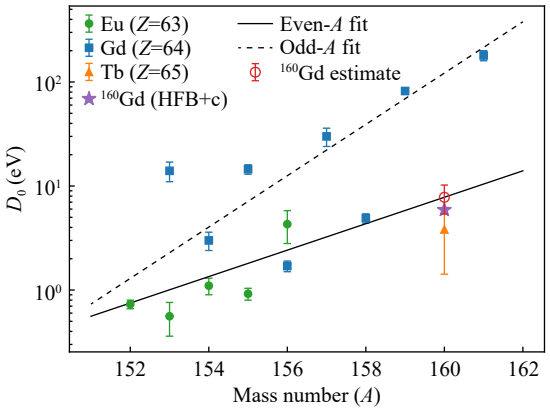

Fig. 3 Systematics of D_0 for Gd isotopes and neighboring nuclei. The experimental data for Eu, Gd, and Tb are shown as green circles, blue squares, and orange triangles, respectively. The black solid line corresponds to the fit for even-A nuclei, while the dashed line indicates the odd-A fit. The red open circle with error bar marks represent the estimated D_0 for ^{160}Gd from the even-A fit. The lavender star denotes the theoretical D_0 value for ^{160}Gd derived from the $\rho(S_n)$ predicted by the microscopic HFB+c model.

We adopt the HFB+c level densities provided by Goriely *et al.* [47] and renormalize them via a Bayesian optimization (BO) method as follows:

$$\rho_{\mathrm{norm}}(E_x,J,\pi) = \exp(c\sqrt{E_x-\delta})\rho_{\mathrm{HFB}}(E_x-\delta,J,\pi), \quad (9)$$

where δ is an energy shift, and constant c acts as a slope correction, playing a role similar to that of the NLD parameter a of phenomenological models.

The optimal values of parameters c and δ are determined through BO, with the objective of simultaneously satisfying two constraints. Specifically, at low excitation energies ($1.05 \le E_x \le 2.05$ MeV), ρ_{norm} is fitted to level densities calculated from known levels using the binning method. The low-energy level density is defined as $\rho(E_{\mathrm{center}}) = \Delta N/\Delta E$, where ΔN is the number of levels in a bin of width $\Delta E = 0.1$ MeV centered at E_{center}. Simultaneously, at S_n, ρ_{norm} is fitted to the $\rho(S_n)$ calculated from Eq. (8). To achieve this, we employ a Gaussian

Table 2 Optimized parameters for the HFB+c level density renormalization, Eq. (9), for ^{154,156,158,160}Gd.

Isotope	ρ_{FG05}		ρ_{FG09}	
	c	δ (MeV)	c	δ (MeV)
^{154}Gd	0.556	–0.263	0.330	–0.740
^{156}Gd	0.781	0.015	0.718	–0.309
^{158}Gd	0.711	0.107	0.378	–0.356
^{160}Gd	0.596	0.131	0.330	–0.507

process surrogate model, minimizing the total χ^2 of both constraints. The search ranges for parameters c and δ are both set to $[-1.5, 1.5]$. The optimization is performed independently for the ρ_{FG05} and ρ_{FG09} of $\rho(S_n)$, yielding two (c, δ) parameter sets per isotope. These define the NLD uncertainty band. Final optimized parameters are listed in Table 2. As expected, ρ_{FG05} yields more positive δ and larger c than ρ_{FG09}, since a larger target value requires a steeper level density curve. Figure 4 shows a fit for ^{156}Gd as an example, where the renormalized curves reproduce the low-energy discrete levels while passing through the respective $\rho(S_n)$ anchors. Similar fit quality is obtained for the other isotopes. The uncertainty band bounded by these two curves is propagated to the cross section calculations.

3 Cross section calculations

The (n,γ) cross sections in TALYS are calculated within the Hauser–Feshbach (HF) statistical model [48] and depend on the neutron and γ-ray transmission coefficients [21, 22]. In the energy region just above the resonance range and before the opening of the inelastic channel, the neutron transmission coefficient is much larger than the γ-ray transmission coefficient. In this case, the HF expression can be written as

$$\sigma_{n,\gamma}(E_n) = \frac{T_n T_\gamma}{T_n + T_\gamma} \approx T_\gamma, \tag{10}$$

where T_n and T_γ denote the neutron and total γ-ray transmission coefficients, respectively. T_n is determined by the neutron optical model potential (OMP), and in the present work it is calculated using the Koning–Delaroche (KD) [49] OMP. T_γ can be written as

$$T_\gamma = \sum_{J,\pi} \sum_{X\ell} \sum_{I'=|J-\ell|}^{J+\ell} \sum_{\pi'} \int_0^{S_n} \mathrm{d}E_\gamma \, 2\pi E_\gamma^{2\ell+1} f_{X\ell}(E_\gamma) \times \rho(S_n - E_\gamma, I', \pi') \, F(X, \pi', \ell), \tag{11}$$

where I' and π' denote the spin and parity of the final states, respectively, and $F(X, \Pi', \ell)$ is the selection-rule factor. In the present work, the E1 γSF is given by Eq. (1), and ρ is taken from the renormalized HFB+c level densities obtained using Eq. (9). Therefore, the calculated (n,γ) cross sections depend explicitly on the γSF and the NLD, and the corresponding uncertainties are propagated through $f_{X\ell}(E_\gamma)$ and ρ. The calculation procedure is summarized as follows:

(i) Cross sections were calculated using the combinations of NLD and γSF (both $E1$ and $M1$ components) models provided in TALYS. This procedure yields an estimate of the model uncertainty range, defined by the lower and upper limits from the theoretical models, for all isotopes studied here.

(ii) Cross sections were calculated using the default models and parameters in TALYS.

(iii) Cross sections and reaction rates were calculated by implementing the constrained γSF and NLD parameters. The results for the stable isotopes ^{155,157}Gd serve as a validation, supporting the reliability of the predictions for the unstable isotopes ^{153,159}Gd.

3.1 Cross sections predictions for model uncertainties

We performed calculations for various combinations of the available NLD models and γSF prescriptions ($E1$ and $M1$) in TALYS. In these calculations, the KD OMP [49] was adopted. To assess the sensitivity of the inferred data to the choice of OMP, we compared the

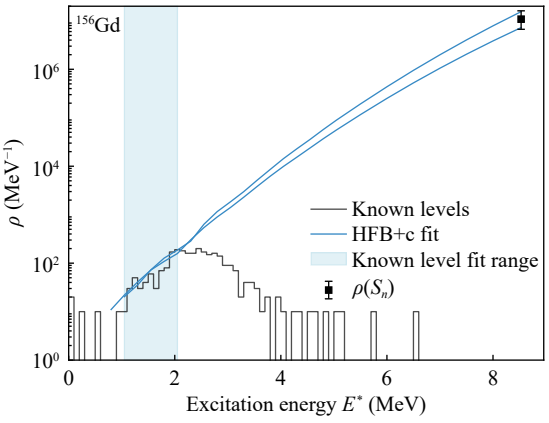

Fig. 4 NLD for ^{156}Gd, as an example. The known discrete levels are plotted as a black solid line. The upper and lower bounds of our renormalized HFB+c NLD are shown as two blue solid lines. The light blue shaded area indicates the energy range of the discrete levels used to fit. The $\rho(S_n)$ is shown as a black square with error bars.

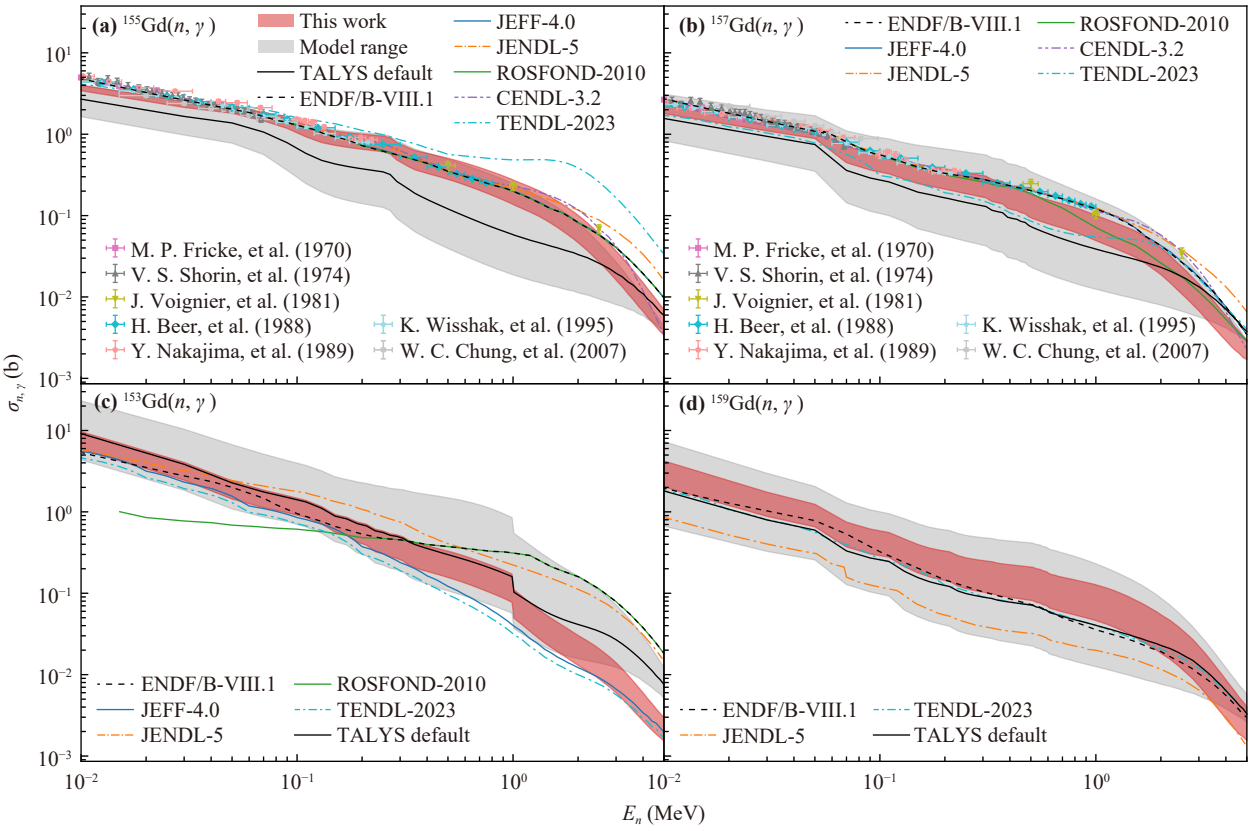

Fig. 5 **(a–d)** show the (n,γ) cross sections of ^{155,157,153,159}Gd. The experimental datasets [5, 54–59] and main evaluation (ENDF/B-VIII.1, JEFF-4.0, JENDL-5, TENDL-2023, ROSFOND-2010, CENDL-3.2) [60–65] are presented. The solid black lines represent the default prediction of TALYS. The red shaded bands represent the results of this work. The gray shaded bands show the model uncertainty range from various combinations of NLD, $E1$ γSF, and $M1$ γSF models available in TALYS.

results obtained with the KD and Jeukenne–Lejeune–Mahaux (JLM) [50] OMPs. The calculated results show that the data obtained with the KD potential is slightly higher (by a factor of 1.2) than those obtained with the JLM potential. Since this sensitivity is relatively modest, in the following we employ the KD OMP by default to calculate the $(n,\ \gamma)$ cross sections of the above-mentioned four Gd isotopes. The resulting uncertainty range is shown as the gray shaded bands in Fig. 5. The combinations yielding the minimum and maximum values are:

(i) Minimum cross section: calculated using the temperature-dependent RMF $E1$ strength function model from Daoutidis and Goriely [51], the SLO $M1$ strength function based on the RIPL-3 systematic formulae [22], and the constant temperature + Fermi gas model for the NLD as introduced by Gilbert and Cameron [52] (TALYS keywords `strength 7`, `strengthM1 1`, `ldmodel 1`).

(ii) Maximum cross section: calculated using the Brink-Axel Lorentzian $E1$ strength function [29, 30], the $M1$ strength function including spin-flip and scissors-mode contributions, and the NLD is based on temperature-dependent Hartree–Fock–Bogoliubov calculations using the Gogny force [53] (TALYS keywords `strength 2`, `strengthM1 3`, `ldmodel 6`).

To characterize the uncertainty of the inferred cross sections, we define the uncertainty interval as $(\sigma_{\max,i}-\sigma_{\min,i})/2\langle\sigma_i\rangle$, where $\sigma_{\max,i}$, $\sigma_{\min,i}$, and $\langle\sigma_i\rangle$ denote the maximum, minimum, and mean (n,γ) cross sections for a given isotope at the i-th neutron-energy point. Using various combinations of NLD, $E1$, and $M1$ γSF models in TALYS, the uncertainty intervals over E_n = 0.01–5 MeV are calculated to be 68.26%–89.73% for ^{153}Gd, 45.64%–88.59% for ^{155}Gd, 63.03%–93.01% for ^{157}Gd, and 76.11%–90.28% for ^{159}Gd. These results underscore the importance of experimental constraints on both the γSF and NLD to reduce the inherent model uncertainties in cross section predictions. This is particularly relevant for the energy region that dominates astrophysical s-process conditions and thermal reactor applications.

To further assess the sensitivity of the calculated cross sections to individual model components, we varied the γSF and NLD models separately while keeping the other model components fixed, with the uncertainty factor is

defined as the ratio of the maximum to minimum cross sections. In the E_n = 0.01–5 MeV energy range, NLD variations yield an average uncertainty factor of ∼2.8 for the four Gd isotopes. The largest factors are obtained for ^{157,159}Gd, reaching 3.4 and 3.2, respectively. The $E1$ γSF produces an average uncertainty factor of ∼3.3, ranging from 2.7 for ^{153}Gd to 4.4 for ^{159}Gd. In contrast, the $M1$ strength function has a minimal impact, with a factor of only 1.1. This is attributed to the significantly smaller magnitude of the $M1$ strength compared to the dominant $E1$ component, thereby limiting its influence on the (n,γ) cross sections.

3.2 TALYS default predictions

For comparison, we also performed calculations using the default models and parameters of TALYS. These are the Simplified Modified Lorentzian model [66] for $E1$ γSF, the Spin-flip and scissors mode for $M1$ γSF [40], and the Constant Temperature + Fermi gas model [67] for the NLD. The results are displayed as black lines in Fig. 5. For the stable isotopes ^{155,157}Gd, significant discrepancies are observed between the TALYS default predictions and the experimental data. For ^{153}Gd, the TALYS default prediction is higher than the major evaluated libraries when $E_n < 0.04$ MeV. In the high-energy region, the TALYS default falls in between the evaluated libraries. For ^{159}Gd, the TALYS default prediction is in good agreement with the ENDF/B-VIII.1 and TENDL-2023 libraries.

3.3 Results from constrained nuclear model parameters

Finally, we employ our constrained nuclear model parameters to calculate the ^{153,155,157,159}Gd(n,γ) cross sections. For the neutron transmission coefficients, we adopted the KD optical potential [49]. The total uncertainty in our results accounts for three contributions: (i) $E1$ γSF: Uncertainties are propagated via Monte Carlo sampling of the double-Lorentzian parameters (Table 1) based on their covariance matrix. (ii) $M1$ γSF: The uncertainty is defined by the envelope of predictions from the three phenomenological models discussed in Section 2.2. (iii) NLD: The uncertainty is propagated from the renormalized NLD bands derived in Section 2.3 (Table 2).

We first calculate the cross sections for stable isotopes ^{155,157}Gd(n,γ), for which abundant experimental data exist, to validate our approach. As shown in Figs. 5(a) and (b), for the stable isotope ^{155}Gd, our results show good agreement with both experimental data and most of the evaluated libraries across the entire energy range. The only exception is TENDL-2023, which begins to deviate from our results above 0.1 MeV. Similarly, for ^{157}Gd, our predictions agree well with the experimental data although they are slightly lower than part of the dataset. Based on this, we further calculate the ^{153,159}Gd(n,γ) cross sections, where no experimental data are available. As shown in Figs. 5(c) and (d), for ^{153}Gd, our calculated cross sections are consistent with the ENDF/B-VIII.1 evaluation below 0.3 MeV. In the energy range of 0.3–1.2 MeV, our results lie between the JEFF-4 and JENDL-5 predictions. Above 1.2 MeV, our calculations agree well with TENDL-2023 and JEFF-4. Finally, for ^{159}Gd, our calculations are slightly higher than most evaluations across the considered energy range. However, the lower bound of our calculated band shows good agreement with ENDF/B-VIII.1 and TENDL-2023. Overall, the uncertainty intervals of the extracted ^{153,155,157,159}Gd data over E_n = 0.01–5 MeV are estimated to be 23.54%–40.37%, 7.63%–39.38%, 14.32%–36.64%, and 30.82%–51.05%, respectively. These uncertainties are narrower than those obtained with the TALYS models without experimental constraints.

4 Astrophysical implication

Based on the constrained cross sections, we calculate the astrophysical reaction rates for ^{153,159}Gd(n,γ), as shown in Fig. 6(a). These are compared with the recommended values from the JINA REACLIB database [68]. Note that the *ks03* evaluation [69] is used for ^{153}Gd and the *thra* evaluation [70] is used for ^{159}Gd in the database. For ^{153}Gd, the JINA recommended values agree with the upper limit of our uncertainty band. In contrast, our calculated rates for ^{159}Gd are notably higher than the JINA REACLIB recommended values, approximately by a factor of 2.9 at the mean value. The enhanced (n,γ) rate found in this work implies a stronger reaction flux through this channel than JINA REACLIB estimated, potentially facilitating the synthesis of heavier isotopes such as ^{160}Gd.

4.1 The branching at ^{153}Gd and ^{159}Gd

As mentioned in Section 1, the final abundances of the s-only Gd isotopes are sensitive to branchings at unstable nuclei, where neutron capture competes with β decay. We investigate the branchings at ^{153}Gd and ^{159}Gd, which influence the production of the s-only isotope ^{154}Gd and the s-process contribution to ^{160}Gd, respectively. This competition can be quantified by the neutron capture branching ratio $f_{n,\gamma}$, defined as

$$f_{n,\gamma} = \frac{\lambda_{n,\gamma}}{\lambda_{n,\gamma} + \lambda_\beta} = \frac{n_n \langle \sigma v \rangle}{n_n \langle \sigma v \rangle + \ln 2 / t_{1/2}}. \tag{12}$$

Here, $\lambda_{n,\gamma}$ and λ_β denote the rates for neutron capture and β-decay, respectively. The n_n is the neutron density, and $t_{1/2}$ is the β-decay half-life. The $\langle \sigma v \rangle$ denotes the reaction rate per particle pair (in $\mathrm{cm}^3 \cdot \mathrm{s}^{-1}$). Note that the astrophysical reaction rates presented in

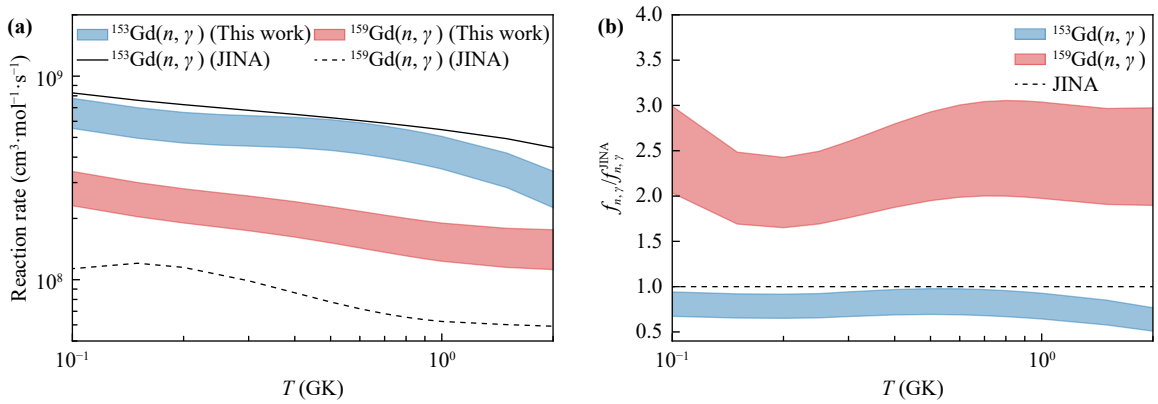

Fig. 6 **(a, b)** show the astrophysical reaction rates and the $f_{n,\gamma}$ relative to JINA REACLIB, as a function of temperature, respectively. The blue shaded bands denote and the red shaded bands denote the ^{153,159}Gd(n,γ) result obtained in this work, respectively. In panel (a), the black solid and dashed lines show the JINA REACLIB recommendation for ^{153}Gd and ^{159}Gd, respectively. In panel (b), the horizontal dashed line at unity indicates agreement with JINA REACLIB.

Fig. 6(a) are given as $N_A\langle\sigma v\rangle$ (in $\mathrm{cm^3\cdot mol^{-1}\cdot s^{-1}}$), and thus must be divided by Avogadro's constant N_A for the evaluation of Eq. (12).

We calculated $f_{n,\gamma}$ over the temperature range of 0.1–2 GK, with a typical s-process neutron density of $n_n = 10^8\,\mathrm{cm^{-3}}$. The ratios $f_{n,\gamma}/f_{n,\gamma}^{\mathrm{JINA}}$ for ^{153}Gd and ^{159}Gd are shown in Fig. 6(b). For ^{153}Gd ($t_{1/2} = 240.4$ d), we obtain $f_{n,\gamma} \approx 70\%$ at $T = 0.2$ GK, meaning that neutron capture is the dominant channel, and the ratio $f_{n,\gamma}/f_{n,\gamma}^{\mathrm{JINA}}$ remains close to unity. In contrast, for ^{159}Gd ($t_{1/2} = 18.5$ h), the short half-life leads to a much smaller branching ratio, $f_{n,\gamma} \approx 0.3\%$ at $T = 0.2$ GK, i.e., β decay dominates. Nevertheless, our constrained rates yield a larger branching ratio by a factor of about 2–3 compared to JINA REACLIB. This notable enhancement suggests a stronger neutron-capture flow toward ^{160}Gd compared to the JINA REACLIB prediction.

4.2 Impact on ^{160}Gd production

The enhanced branching at ^{159}Gd is expected to increase the s-process flow toward ^{160}Gd. To illustrate this sensitivity, we perform nucleosynthesis calculations as described below. We performed s-process nucleosynthesis simulations using the single-zone reaction network code `NucNet Tools` [71]. The calculations adopted fixed temperature, density, and neutron abundance. Specifically, the temperature was maintained at $T = 0.2$ GK, and the matter density was set to $\rho = 10^3$ g/cm^3. The neutron abundance was fixed at $Y_n = 1.66 \times 10^{-19}$, corresponding to approximately $n_n \approx 10^8$ cm^{-3}. The solar system elemental abundances from Ref. [72] were adopted as the initial composition. The reaction network was evolved for a duration of 3.15×10^{12} s ($\approx 10^5$ yr), sufficient to reach equilibrium for the relevant isotopes.

As shown in Fig. 7, within the adopted single-zone calculation the ^{160}Gd abundance predicted in this work is consistently higher than the default prediction based on the JINA REACLIB rate after 2×10^{-2} Myr. In the intermediate and late stages of the evolution, our results exhibit a stable enhancement, stabilizing at a factor of approximately 2 compared to the default calculation. However, it should be noted that the above ^{160}Gd abundance enhancement can only be regarded as a trend observed in the present sensitivity study, not yet a definitive prediction for realistic stellar models.

5 Summary and outlook

In summary, we have successfully inferred the unstable ^{153,159}Gd(n,γ) cross sections by constraining the key γSF and NLD inputs. Over $E_n = 0.01$–5 MeV, the uncertainty intervals for these inferred data are evaluated to be

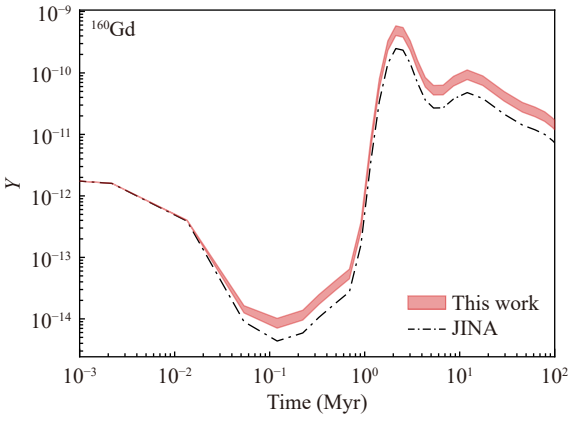

Fig. 7 Evolution of ^{160}Gd abundances in the adopted single-zone s-process calculation. The red shaded band shows results using our updated (n,γ) reaction rates, while the black dash-dotted line represents the calculation based on the JINA REACLIB rate.

23.5%–40.4% for ^{153}Gd and 30.8%–51.1% for ^{159}Gd, which are approximately half of those obtained without experimental constraints. Note that constraining these uncertainties is particularly is particularly important for investigating s-process branching points and the i-process, where experimental data are scarce, but accurate cross sections are essential. Furthermore, we derived the astrophysical reaction rates for ^{153,159}Gd isotopes. The calculated ^{153}Gd(n,γ) reaction rate is comparable to the JINA REACLIB recommendation, while that for ^{159}Gd(n,γ) is higher by a factor of ∼2.9. This is expected to be associated with a larger branching ratio for ^{159}Gd, which in turn results in an approximately twofold increase in the ^{160}Gd abundance through neutron capture reaction in our simplified one-zone setup.

Our study enriches the (n,γ) data for the Gd isotopic chain, thereby providing useful input for astrophysical reaction-network calculations and related applications involving Gd isotopes. In the future, we will apply our approach to derive (n,γ) cross sections for other unstable isotopic chains. Sm and Er isotopes are of our priority, since their (n,γ) data play an important role in determining cosmic-ray exposure conditions for planetary materials [73]. Moreover, their accurate astrophysical reaction rates are indispensable for resolving the competition between (n,γ) reactions and β-decays during the r-process freeze-out, which shapes the final rare-earth abundance pattern [74]. We also should note that in order to infer the (n,γ) data for these unstable isotopes of interest, we still need reliable experimental data of neighboring stable isotopes, which are useful for constraints of their γSFs and NLDs. As a result, we call for more experimental measurements on (n,γ) cross sections at operational and under-construction facilities including CSNS [75, 76], n_TOF [77], LANSCE [78], J-PARC [79], GELINA [80], and SARAF-II [81].

Declarations The authors declare that they have no competing interests and there are no conflicts.

Acknowledgements This work was supported by the National Key R&D Program of China (Grant No. 2022YFA1603300) and the National Natural Science Foundation of China (Grant Nos. 12575133 and 12505144).

References

1. M. R. Mumpower, R. Surman, G. C. McLaughlin, and A. Aprahamian, The impact of individual nuclear properties on r-process nucleosynthesis, *Prog. Part. Nucl. Phys.* 86, 86 (2016)
2. A. Arcones, D. W. Bardayan, T. C. Beers, L. A. Bernstein, J. C. Blackmon, et al., White paper on nuclear astrophysics and low energy nuclear physics Part 1: Nuclear astrophysics, *Prog. Part. Nucl. Phys.* 94, 1 (2017)
3. B. Burbidge, G. Burbidge, W. A. Fowler, and F. Hoyle, Synthesis of the elements in stars, *Rev. Mod. Phys.* 29(4), 547 (1957)
4. A. Mazzone, S. Cristallo, O. Aberle, G. Alaerts, V. Alcayne, et al., Measurement of the ^{154}Gd(n,γ) cross section and its astrophysical implications, *Phys. Lett. B* 804, 135405 (2020)
5. K. Wisshak, F. Voss, F. Käppeler, K. Guber, L. Kazakov, N. Kornilov, M. Uhl, and G. Reffo, Stellar neutron capture cross sections of the Gd isotopes, *Phys. Rev. C* 52(5), 2762 (1995)
6. C. Massimi, Measurement of the neutron capture cross section of gadolinium even isotopes relevant to Nuclear Astrophysics, Tech. Rep., CERN, Geneva, 2015
7. N. D. Scielzo, L. A. Bernstein, D. L. Bleuel, J. T. Burke, et al., in: AIP Conference Proceedings, Vol. 1005, AIP, Yosemite National Park (California), 2008, pp 109–112
8. Y. R. Kang, M. W. Lee, G. N. Kim, T. I. Ro, Y. Danon, D. Williams, G. Leinweber, R. C. Block, D. P. Barry, and M. J. Rapp, Neutron capture measurements and resonance parameters of gadolinium, *Nucl. Sci. Eng.* 180(1), 86 (2015)
9. R. Q. Wright, Revised Evaluations for ENDF/B-VI Revision 2, Oak Ridge National Lab., TN (United States), 1993
10. S. L. Ho, H. Yue, T. Tegafaw, M. Y. Ahmad, S. Liu, S. W. Nam, Y. Chang, and G. H. Lee, Gadolinium neutron capture therapy (GdNCT) agents from molecular to nano: Current status and perspectives, *ACS Omega* 7(3), 2533 (2022)
11. A. Ratkiewicz, J. A. Cizewski, J. E. Escher, G. Potel, J. T. Harke, R. J. Casperson, M. McCleskey, R. A. E. Austin, S. Burcher, R. O. Hughes, B. Manning, S. D. Pain, W. A. Peters, S. Rice, T. J. Ross, N. D. Scielzo, C. Shand, and K. Smith, Towards neutron capture on exotic nuclei: Demonstrating $(d, p\gamma)$ as a surrogate reaction for (n,γ), *Phys. Rev. Lett.* 122(5), 052502 (2019)
12. A. Thapa, J. Escher, E. Chimanski, O. Gorton, M. Dupuis, E. J. In, S. Ota, S. Péru, and W. Younes, Constraining capture cross sections using proton inelastic scattering as a surrogate reaction, arXiv: 2511.03071 [nucl-th] (2025)
13. S. N. Liddick, A. Spyrou, B. P. Crider, F. Naqvi, A. C. Larsen, M. Guttormsen, M. Mumpower, R. Surman, G. Perdikakis, D. L. Bleuel, A. Couture, L. Crespo Campo, A. C. Dombos, R. Lewis, S. Mosby, S. Nikas, C. J. Prokop, T. Renstrom, B. Rubio, S. Siem, and S. J. Quinn, Experimental neutron capture rate constraint far from stability, *Phys. Rev. Lett.* 116(24), 242502 (2016)
14. M. Arnould, S. Goriely, and K. Takahashi, The r-process of stellar nucleosynthesis: Astrophysics and nuclear physics achievements and mysteries, *Phys. Rep.* 450(4-6), 97 (2007)
15. R. Pérez Sánchez, B. Jurado, V. Méot, O. Roig, M. Dupuis, O. Bouland, D. Denis-Petit, P. Marini, L. Mathieu, I. Tsekhanovich, M. Aïche, L. Audouin, C. Cannes, S. Czajkowski, S. Delpech, A. Görgen, M. Guttormsen, A. Henriques, G. Kessedjian, K. Nishio, D.

Ramos, S. Siem, and F. Zeiser, Simultaneous determination of neutron-induced fission and radiative capture cross sections from decay probabilities obtained with a surrogate reaction, *Phys. Rev. Lett.* 125(12), 122502 (2020)
16. S. T. Zhang, W. Luo, D. Y. Pang, Z. C. Li, et al., Constraining neutron capture cross sections for ^{88}Y with gamma-ray strength function in (p, $p'\gamma$) surrogate reaction, arXiv: 2511.10955 [nucl-th] (2025)
17. J. E. Escher, J. T. Harke, R. O. Hughes, N. D. Scielzo, R. J. Casperson, S. Ota, H. I. Park, A. Saastamoinen, and T. J. Ross, Constraining neutron capture cross sections for unstable nuclei with surrogate reaction data and theory, *Phys. Rev. Lett.* 121(5), 052501 (2018)
18. A. C. Larsen, A. Spyrou, S. N. Liddick, and M. Guttormsen, Novel techniques for constraining neutron-capture rates relevant for r-process heavy-element nucleosynthesis, *Prog. Part. Nucl. Phys.* 107, 69 (2019)
19. M. Sguazzin, B. Jurado, J. Pibernat, J. A. Swartz, M. Grieser, et al., First measurement of the neutron-emission probability with a surrogate reaction in inverse kinematics at a heavy-ion storage ring, *Phys. Rev. Lett.* 134(7), 072501 (2025)
20. M. Sguazzin, B. Jurado, J. Pibernat, J. A. Swartz, M. Grieser, et al., First simultaneous measurement of the γ-ray and neutron emission probabilities in inverse kinematics at a heavy-ion storage ring, *Phys. Rev. C* 111(2), 024614 (2025)
21. A. Koning, S. Hilaire, and S. Goriely, TALYS: modeling of nuclear reactions, *Eur. Phys. J. A* 59(6), 131 (2023)
22. R. Capote, M. Herman, P. Obložinský, P. G. Young, S. Goriely, et al., RIPL – Reference input parameter library for calculation of nuclear reactions and nuclear data evaluations, *Nucl. Data Sheets* 110(12), 3107 (2009)
23. S. Goriely, P. Dimitriou, M. Wiedeking, T. Belgya, R. Firestone, J. Kopecky, M. Krtička, V. Plujko, R. Schwengner, S. Siem, H. Utsunomiya, S. Hilaire, S. Péru, Y. S. Cho, D. M. Filipescu, N. Iwamoto, T. Kawano, V. Varlamov, and R. Xu, Reference database for photon strength functions, *Eur. Phys. J. A* 55(10), 172 (2019)
24. O. V. Vasilev, V. A. Semenov, and S. F. Semenko, Giant dipole resonance on nuclei in transition region n approximately 90, *Yadern. Fiz.* 13, 463 (1971)
25. L. M. Bollinger and G. E. Thomas, Average-resonance method of neutron-capture γ-ray spectroscopy: States of ^{106}Pd, ^{156}Gd, ^{158}Gd, ^{166}Ho, and ^{168}Er, *Phys. Rev. C.* 2(5), 1951 (1970)
26. G. Gurevich, L. Lazareva, V. Mazur, S. Merkulov, G. V. Solodukhov, and V. A. Tyutin, Total nuclear photoabsorption cross sections in the region $150 < A < 190$, *Nucl. Phys. A* 351(2), 257 (1981)
27. B. L. Berman, M. A. Kelly, R. L. Bramblett, J. T. Caldwell, H. S. Davis, and S. C. Fultz, Giant resonance in deformed nuclei: photoneutron cross sections for ^{153}Eu, ^{160}Gd, ^{165}Ho, and ^{186}W, *Phys. Rev.* 185, 1576 (1969)
28. R. Greenwood, C. Reich, H. Baader, H. Koch, et al., Collective and two-quasiparticle states in 158Gd observed through study of radiative neutron capture in ^{157}Gd, *Nucl. Phys. A* 304(2), 327 (1978)
29. D. Brink, Individual particle and collective aspects of the nuclear photo effect, *Nucl. Phys.* 4, 215 (1957)
30. P. Axel, Electric dipole ground-state transition width strength function and 7 MeV photon interactions, *Phys. Rev.* 126(2), 671 (1962)
31. G. A. Bartholomew, E. D. Earle, A. J. Ferguson, J. W. Knowles, et al., in: Advances in Nuclear Physics, Springer US, Boston, MA, 1973, pp 229–324
32. B. L. Berman and S. C. Fultz, Measurements of the giant dipole resonance with monoenergetic photons, *Rev. Mod. Phys.* 47(3), 713 (1975)
33. S. S. Dietrich and B. L. Berman, Atlas of photoneutron cross sections obtained with monoenergetic photons, *At. Data Nucl. Data Tables* 38(2), 199 (1988)
34. S. Goriely, N. Chamel, and J. M. Pearson, Skyrme-Hartree–Fock–Bogoliubov nuclear mass formulas: Crossing the 0.6 MeV accuracy threshold with microscopically deduced pairing, *Phys. Rev. Lett.* 102(15), 152503 (2009)
35. E. G. Fuller and M. S. Weiss, Splitting of the giant resonance for deformed nuclei, *Phys. Rev.* 112(2), 560 (1958)
36. S. Goriely, E. Khan, and M. Samyn, Microscopic HFB + QRPA predictions of dipole strength for astrophysics applications, *Nucl. Phys. A* 739(3–4), 331 (2004)
37. S. Goriely, S. Hilaire, S. Péru, and K. Sieja, Gogny-HFB+QRPA dipole strength function and its application to radiative nucleon capture cross section, *Phys. Rev. C* 98(1), 014327 (2018)
38. M. Danos, On the long-range correlation model of the photonuclear effect, *Nucl. Phys.* 5, 23 (1958)
39. T. Belgya, O. Bersillon, R. C. Noy, T. Fukahori, et al., Handbook for calculations of nuclear reaction data. IAEAtechdoc, 2004
40. N. L. Iudice and F. Palumbo, New isovector collective modes in deformed nuclei, *Phys. Rev. Lett.* 41(22), 1532 (1978)
41. D. Bohle, A. Richter, W. Steffen, A. Dieperink, N. Lo Iudice, F. Palumbo, and O. Scholten, New magnetic dipole excitation mode studied in the heavy deformed nucleus ^{156}Gd by inelastic electron scattering, *Phys. Lett. B* 137(1–2), 27 (1984)
42. M. R. Mumpower, T. Kawano, J. L. Ullmann, M. Krtička, and T. M. Sprouse, Estimation of M1 scissors mode strength for deformed nuclei in the medium- to heavy-mass region by statistical Hauser–Feshbach model calculations, *Phys. Rev. C* 96(2), 024612 (2017)
43. A. C. Larsen, M. Guttormsen, R. Schwengner, D. L. Bleuel, S. Goriely, S. Harissopulos, F. L. Bello Garrote, Y. Byun, T. K. Eriksen, F. Giacoppo, A. Görgen, T. W. Hagen, M. Klintefjord, T. Renstrøm, S. J. Rose, E. Sahin, S. Siem, T. G. Tornyi, G. M. Tveten, A. V. Voinov, and M. Wiedeking, Experimentally constrained (p, γ) ^{89}Y and (n, γ) ^{89}Y reaction rates relevant to p-process nucleosynthesis, *Phys. Rev. C* 93(4), 045810 (2016)
44. T. V. Egidy and D. Bucurescu, Systematics of nuclear level density parameters, *Phys. Rev. C* 72(4), 044311 (2005)
45. T. von Egidy and D. Bucurescu, Experimental energy-dependent nuclear spin distributions, *Phys. Rev. C*

80(5), 054310 (2009)
46. T. Ericson, A statistical analysis of excited nuclear states, *Nucl. Phys.* 11, 481 (1959)
47. S. Goriely, S. Hilaire, and A. J. Koning, Improved microscopic nuclear level densities within the Hartree-Fock-Bogoliubov plus combinatorial method, *Phys. Rev. C* 78(6), 064307 (2008)
48. W. Hauser and H. Feshbach, The inelastic scattering of neutrons, *Phys. Rev.* 87(2), 366 (1952)
49. A. Koning and J. Delaroche, Local and global nucleon optical models from 1 keV to 200 MeV, *Nucl. Phys. A* 713(3-4), 231 (2003)
50. E. Bauge, J. P. Delaroche, and M. Girod, Lane-consistent, semimicroscopic nucleon-nucleus optical model, *Phys. Rev. C* 63(2), 024607 (2001)
51. I. Daoutidis and S. Goriely, Large-scale continuum random-phase approximation predictions of dipole strength for astrophysical applications, *Phys. Rev. C* 86(3), 034328 (2012)
52. A. Gilbert and A. G. W. Cameron, A composite nuclear-level density formula with shell corrections, *Can. J. Phys.* 43(8), 1446 (1965)
53. S. Hilaire, M. Girod, S. Goriely, and A. J. Koning, Temperature-dependent combinatorial level densities with the D1M Gogny force, *Phys. Rev. C Nucl. Phys.* 86(6), 064317 (2012)
54. Y. Nakajima, I. Tsubone, M. Mizumoto, Y. Furuta, M. Ohkubo, M. Sugimoto, and Y. Kawarasaki, Neutron capture cross section measurements of ^{155}Gd and ^{157}Gd from 1.1 to 235 keV, *Ann. Nucl. Energy* 16(11), 589 (1989)
55. J. Voignier, S. Joly, and G. Grenier, Neutron capture cross section measurements of rubidium, yttrium, niobium, gadolinium, tungsten, platinum and thallium between 0.5 and 3.0 MeV, Tech. Rep. CEA-R–5089, CEA Centre d'Etudes de Bruyeres-le-Chatel, Montrouge, France, 1981
56. V. S. Shorin, V. N. Kononov, and E. D. Poletaev, Cross sections of neutron radiative capture in the energy range 5 to 70 keV for Gd and Er isotopes, *Yadern. Fiz.* 19(1), 5 (1974)
57. M. P. Fricke, W. M. Lopez, S. J. Friesenhahn, A. D. Carlson, and D. G. Costello, Measurements of cross-sections for the radiative capture of 1 keV to 1 MeV neutrons by Mo, Rh, Gd, Ta, W, Re, Au and ^{238}U, in: Nuclear Data for Reactors, Vol. 2, IAEA, 1970, pp 265–280
58. H. Beer and R. L. Macklin, The Sm-151 branching - A probe for the irradiation time scale of the *s*-process, *Astrophys. J.* 331, 1047 (1988)
59. W. C. Won-Chung, T. I. Tae-Ik, G. Guinyun, S. Samyol, M. Masayuki, and T. Toshiro, Measurement of the keV-neutron capture cross-sections and capture gamma-ray spectra of ^{155}Gd and ^{157}Gd, *J. Korean Phys. Soc.* 50(2), 409 (2007)
60. G. Nobre, D. Brown, R. Arcilla, R. Coles, and B. Shu, Progress towards the ENDF/B-VIII. 1 release, *EPJ Web Conf.* 294, 04004 (2024)
61. A. J. M. Plompen, O. Cabellos, C. De Saint Jean, M. Fleming, A. Algora, et al., The joint evaluated fission and fusion nuclear data library, JEFF-3.3, *Eur. Phys. J. A* 56(7), 181 (2020)
62. O. Iwamoto, N. Iwamoto, S. Kunieda, F. Minato, S. Nakayama, et al., Japanese evaluated Nuclear Data Library Version 5: JENDL-5, *J. Nucl. Sci. Technol.* 60(1), 1 (2023)
63. S. Zabrodskaya, A. Ignatyuk, V. Koshcheev, et al., Vop. At. Nauki i Tekhn, Ser. Yadernye Konstanty 1–2 (2007)
64. A. Koning, D. Rochman, J. C. Sublet, N. Dzysiuk, M. Fleming, and S. van der Marck, TENDL: Complete nuclear data library for innovative nuclear science and technology, *Nucl. Data Sheets* 155, 1 (2019)
65. Z. Ge, R. Xu, H. Wu, Y. Zhang, G. Chen, Y. Jin, N. Shu, Y. Chen, X. Tao, Y. Tian, P. Liu, J. Qian, J. Wang, H. Zhang, L. Liu, and X. Huang, CENDL-3.2: The new version of Chinese general purpose evaluated nuclear data library, *EPJ Web Conf.* 239, 09001 (2020)
66. V. A. Plujko, Verification of models for calculation of E1 radiative strength function, *PoS* PSF07, 002 (2008)
67. A. Gilbert and A. G. W. Cameron, A composite nuclear-level density formula with shell corrections, *Can. J. Phys.* 43(8), 1446 (1965)
68. R. H. Cyburt, A. M. Amthor, R. Ferguson, Z. Meisel, K. Smith, S. Warren, A. Heger, R. D. Hoffman, T. Rauscher, A. Sakharuk, H. Schatz, F. K. Thielemann, and M. Wiescher, The Jina Reaclib database: Its recent updates and impact on type-I X-ray bursts, *Astrophys. J. Suppl. Ser.* 189(1), 240 (2010)
69. I. Dillmann, R. Plag, F. Käppeler, and T. Rauscher, KADoNiS v0.3 – the third update of the "Karlsruhe Astrophysical Database of Nucleosynthesis in Stars", 2010
70. T. Rauscher and F. K. Thielemann, Astrophysical reaction rates from statistical model calculations, *At. Data Nucl. Data Tables* 75(1–2), 1 (2000)
71. B. S. Meyer, Nucnet-tools, URL: sourceforge.net/projects/nucnet-tools/
72. K. Lodders, Solar system abundances and condensation temperatures of the elements, *Astrophys. J.* 591(2), 1220 (2003)
73. H. Hidaka, Isotopic variations of Sm, Gd, Er and Yb found in planetary materials caused by neutron-capture reactions in nature, *J. Anal. Sci. Technol.* 15(1), 14 (2024)
74. G. G. Kiss, A. Vitéz-Sveiczer, Y. Saito, A. Tarifeño-Saldivia, M. Pallas, et al., Measuring the β-decay properties of neutron-rich exotic Pm, Sm, Eu, and Gd isotopes to constrain the nucleosynthesis yields in the rare-earth region, *Astrophys. J.* 936(2), 107 (2022)
75. H. Chen, and X. L. Wang, China's first pulsed neutron source, *Nat. Mater.* 15(7), 689 (2016)
76. W. Zhou, W. Pan, R. Ge, F. He, J. Dai, Z. Mi, H. Zhao, T. Huang, Q. Ma, S. Jin, M. Xu, M. li, M. Liu, Z. Wang, X. Zhang, X. Wang, L. Ye, B. Liu, H. Liu, Z. Xie, C. Zhang, M. Fan, Z. He, J. Peng, and S. Wang, Development of the double spoke cavity prototype for CSNS-II, *Nucl. Instrum. Methods Phys. Res. A* 1062, 169170 (2024)
77. C. Guerrero, A. Tsinganis, E. Berthoumieux, M. Barbagallo, F. Belloni, et al, Performance of the neutron time-of-flight facility n_TOF at CERN, *Eur. Phys. J. A* 49(2), 27 (2013)

78. M. Heil, R. Reifarth, M. M. Fowler, R. C. Haight, F. Käppeler, R. S. Rundberg, E. H. Seabury, J. L. Ullmann, J. B. Wilhelmy, and K. Wisshak, A 4 detector for (n, γ) cross-section measurements at a spallation neutron source, *Nucl. Instrum. Methods Phys. Res. A* 459(1–2), 229 (2001)
79. M. Igashira, T. Katabuchi, H. Harada, S. Nakamura, A. Kimura, N. Iwamoto, J. Hori, and Y. Kiyanagi, A nuclear data project on neutron capture cross sections of long-lived fission products and minor actinides, *Nucl. Data Sheets* 118, 72 (2014)
80. W. Mondelaers and P. Schillebeeckx, GELINA, a neutron time-of-flight facility for high-resolution neutron data measurements, *Notiziario Neutroni e Luce di Sincrotrone* 11, 19 (2006)
81. B. Kaizer, I. Fishman, A. Perry, L. Weissman, T. Zchut, J. Luner, E. Farber, A. Azoulay, and S. Robin, High power solid state RF amplifiers for SARAF Phase II Linac, *Nucl. Instrum. Methods Phys. Res. A* 1039, 167001 (2022)